

Structural and transport properties of LiTFSI/G₃ electrolyte with machine-learned molecular dynamics

Chenyang Cao,¹ Liyi Bai,² Shuo Cao,³ Ye Su,¹ Yanzhou Wang,⁴ Zheyong Fan,⁵ and Ping Qian^{1,*}

¹*Beijing Advanced Innovation Center for Materials Genome Engineering,
Department of Physics, University of Science and Technology Beijing, Beijing 100083, China*

²*Suzhou Laboratory, Suzhou 215100, China*

³*Beijing Advanced Innovation Center for Materials Genome Engineering,
Corrosion and Protection Center, University of Science and Technology Beijing, Beijing, 100083, China*

⁴*Department of Applied Physics, QTF Center of Excellence,
Aalto University, FIN-00076 Aalto, Espoo, Finland*

⁵*College of Physical Science and Technology, Bohai University, Jinzhou 121013, P. R. China*

(Dated: April 1, 2025)

The lithium bis(trifluoromethylsulfonyl)azanide-triglyme (LiTFSI/G₃) electrolyte plays a critical role in the performance of lithium-ion batteries. However, its solvation structure and transport properties at the atomic scale remain incompletely understood. In this study, we develop an efficient and accurate neuroevolution potential (NEP) model by integrating bootstrap and active learning strategies. Using machine-learned NEP-driven molecular dynamics simulations, we explore the structural and diffusion properties of LiTFSI/G₃ across a wide range of the solute-to-solvent ratios, systematically analyzing electrolyte density, ion coordination, viscosity, and lithium self-diffusion. The computed densities show excellent agreement with experimental data, and pair correlation analysis reveals significant interactions between lithium ions and surrounding oxygen atoms, which strongly impacts Li⁺ mobility. Viscosity and diffusion calculations further demonstrate that increasing LiTFSI concentration enhances Li-O interactions, resulting in higher viscosity and reduced lithium diffusion. Additionally, machine learning-based path integral molecular dynamics (PIMD) simulations confirm the negligible impact of quantum effects on Li⁺ transport. The electrolyte-specific protocol developed in this work provides a systematic framework for constructing high-fidelity machine learning potentials for complex systems.

I. INTRODUCTION

Lithium-ion batteries (LIBs) are essential for modern energy storage, particularly in electric vehicles and portable electronics, due to their high energy density, long cycle life [1], and reliability [2, 3]. The electrolyte, a key component, governs ion transport and electrochemical stability [4], directly influencing battery performance and lifespan [5–7]. Conventional liquid electrolytes, typically consisting of organic solvents (e.g., carbonates) and lithium salts (e.g., Li⁺ bis(trifluoromethylsulfonyl)azanide (LiTFSI)) [8], offer high ionic conductivity and electrode compatibility. However, their volatility, flammability, and limited electrochemical stability present significant challenges, necessitating the development of safer and more efficient alternatives.

Molecular dynamics (MD) simulations provide atomic-scale insights into electrolyte structure [9–12] and transport [1], revealing key mechanisms of ion solvation, diffusion, and viscosity. However, traditional empirical force fields often fail to accurately capture complex intermolecular interactions, leading to discrepancies in predicting key transport properties. Machine-learned potential (MLP), trained on first-principles data, has emerged as a powerful alternative, achieving near-density functional

theory (DFT) accuracy while maintaining computational efficiency. Successfully applied in metals, catalysis [13], and electrolytes [14–17], MLP leverages large datasets and neural networks to accurately model atomic interactions, providing a robust framework for high-fidelity electrolyte simulations.

In this study, we develop a high-accuracy neuroevolution potential (NEP) [18–21] for the LiTFSI–triglyme (G₃) electrolyte using an active learning approach. NEP is a highly efficient machine-learned potential approach with widespread applications in modeling complex materials [22], including ionic diffusion in solid-state electrolytes [23]. The LiTFSI/G₃ system was selected for its significant influence on Li⁺ transport and its favorable electrochemical properties, including high solubility and stability [24, 25]. Specifically, G₃, as a solvent, exhibits low volatility, non-flammability, and strong solvation capability, making it widely used in metal-ion batteries [26, 27]. Meanwhile, LiTFSI, a common lithium salt, strongly dissociates in non-aqueous solvents, with its TFSI[−] anion reducing viscosity and enhancing ionic conductivity [28].

Using this NEP potential, we systematically investigate the structural and transport properties of LiTFSI/G₃ electrolytes, including density, ion coordination, viscosity, and Li⁺ self-diffusion. Our results demonstrate that classical molecular dynamics (CMD) accurately reproduces experimental density trends, and path integral molecular dynamics (PIMD) [29] confirms the

* qianping@ustb.edu.cn

negligible impact of quantum effects on Li^+ transport. Additionally, increasing LiTFSI concentration strengthens ion-ion interactions, leading to higher viscosity and reduced Li^+ diffusion.

II. MODELS AND METHODS

A. Datasets for training the NEP model

We utilize a publicly available, well-established dataset for LiTFSI/ G_3 [30], constructed from extensive MD simulations of the electrolyte solution. This dataset spans six solute-to-solvent molar fractions: LiTFSI/ $\text{G}_3 = 0, 0.2, 0.36, 0.58, 0.82, \text{ and } 1$. Configurations were sampled from CMD trajectories performed in the NPT ensemble at ambient conditions and in the NVT ensemble over a temperature range of 300–500 K for each molar fraction, yielding a total of 4500 LiTFSI/ G_3 configurations. Figure 1 illustrates a representative snapshot of a 460-atom electrolyte solution system with a solute-to-solvent ratio of LiTFSI/ $\text{G}_3 = 1$. The ball-and-stick model highlights the key molecular components: solvent G_3 and solute LiTFSI molecules. Due to the high degree of atomic environment overlap resulting from dense MD sampling, reducing the training set size is essential to enhance data efficiency while preserving configurational diversity.

To address this, we applied principal component analysis (PCA) to all configurations in the public dataset using the PyNEP code [31], reducing the high-dimensional structural data to two principal components, as shown in Fig. 2. The PCA projection of the original dataset, derived from six molar ratios, is visualized using a color bar. We then performed sparsification on these two components and uniformly selected 154 sparse LiTFSI/ G_3 configurations (black dots in Fig. 2).

Moreover, Wang *et al.* extracted LiTFSI/ G_3 structures from short-time MD trajectories (e.g., 10 ps) for their dataset [30], which constrained the exploration of configurational space. To overcome this limitation, we initially trained a preliminary NEP model on the 154 configurations. Leveraging the computational efficiency of NEP, we conducted a longer 10 ns NEP-driven MD simulation, extracting hundreds of frames at equal intervals. By comparing NEP-predicted atomic forces with DFT-calculated forces, we identified and selected 106 frames with the maximum atomic force difference exceeding 0.8 eV/\AA to enhance the sparse dataset.

To further enhance the robustness of the NEP model, we expanded the mass density range by systematically varying the electrolyte box dimensions. The mass density of LiTFSI/ G_3 at room temperature and pressure was adjusted triaxially from -5% to 5% , corresponding to a density range of 85% to 115% , yielding 70 new density-modulated LiTFSI/ G_3 configurations. To account for quantum dynamical effects in electrolyte simulations, we performed PIMD simulations for 1.2 ns at room temperature and pressure for each molar fraction. From these

trajectories, we selected 160 configurations by filtering frames with the maximum atomic force difference exceeding 0.8 eV/\AA relative to DFT single-point calculations. In total, our training set consists of 490 configurations encompassing 238,658 atomic environments.

To assess the NEP model’s robustness in both interpolation and extrapolation, we constructed a test set comprising 126 electrolyte structures. This set includes 60 frames sampled from 10 ns NPT-CMD trajectories and 66 frames from 1.2 ns PIMD trajectories, all at room temperature and pressure.

Finally, we performed single-point density functional theory (DFT) calculations on all structures in both datasets using the VASP package [32]. The electronic structure was described using the projector augmented wave (PAW) method [33, 34] combined with the generalized gradient approximation (GGA) parameterized by Perdew, Burke, and Ernzerhof (PBE) [35]. A single Gamma k -point was employed for Brillouin zone sampling, with Gaussian smearing applied at a width of 0.05 eV . The kinetic energy cutoff for plane wave expansion was set to 600 eV , and the energy convergence threshold was fixed at 10^{-6} eV .

While van-der-Waals (vdW) interactions are essential for accurately describing the structural properties of the LiTFSI/ G_3 electrolyte [30], they were intentionally excluded from our DFT calculations. This strategy aligns with our research design, where MD simulations are conducted using the integrated NEP-D3 [36] approach by combining NEP and the D3 dispersion correction [37] to explicitly handle vdW effects. By implementing long-range dispersion corrections directly within the MD simulations, we can achieve precise modeling of vdW interactions without complicating the construction of the NEP model.

B. The NEP Formalism

The NEP framework [18–21] combines a neural network (NN) architecture with a separable natural evolution strategy (SNES) [38] to represent the potential energy surface and iteratively optimize model training. It employs a feedforward single-hidden-layer NN to construct a local descriptor for a central atom i , with its site energy U_i expressed as:

$$U_i = \sum_{\mu=1}^{N_{\text{neu}}} \omega_{\mu}^{(1)} \tanh \left(\sum_{\nu=1}^{N_{\text{des}}} \omega_{\mu\nu}^{(0)} q_{\nu}^i - b_{\mu}^{(0)} \right) - b^{(1)}. \quad (1)$$

Here, q_{ν}^i represents the ν -th descriptor component of atom i , and $\tanh(x)$ is the activation function in the hidden layer. The parameters $\omega_{\mu\nu}^{(0)}$ and $b_{\mu}^{(0)}$ define the regression matrix and bias, mapping the ν -th descriptor component to the μ -th neuron in the hidden layer. Similarly, $\omega_{\mu}^{(1)}$ and $b^{(1)}$ map the hidden layer output to U_i .

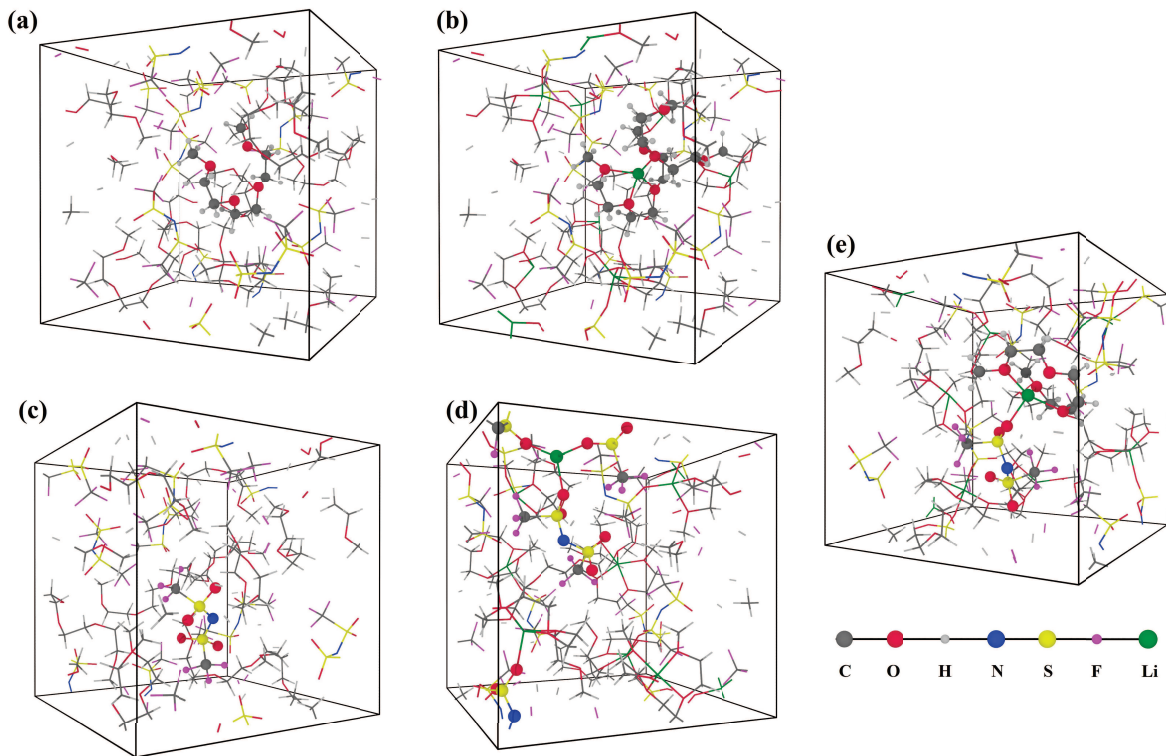


FIG. 1. Snapshots of a 460-atom electrolyte solution system with a solute-to-solvent ratio of $\text{LiTFSI}/\text{G}_3 = 1$. The ball-and-stick model highlights: (a) one G_3 molecule, (b) one Li^+ cation bonded to four oxygen atoms from two neighboring G_3 molecules, (c) one TFSI^- anion, (d) one Li^+ cation bonded to three oxygen atoms from two neighboring TFSI^- anions, and (e) one Li^+ cation bonded to one oxygen atoms from one TFSI^- anion and to two oxygen atoms from one solvent G_3 molecule. The Li-O bonding is cut within 2.3 \AA . C, O, H, N, S, F, and Li atoms are represented by dark grey, red, light grey, blue, yellow, pink, and green spheres, respectively.

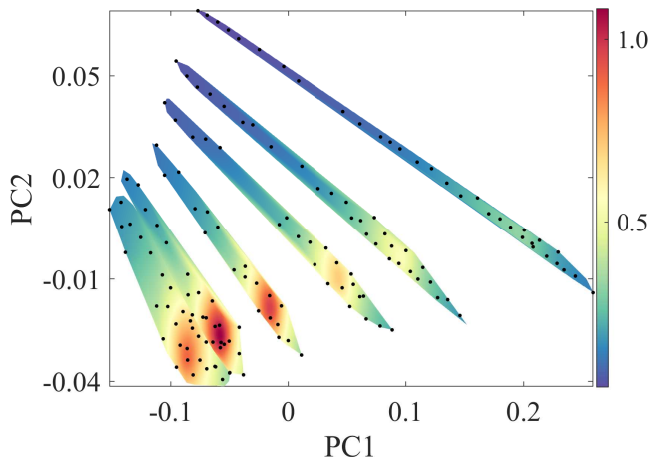


FIG. 2. Principal component analysis (PCA) of the public electrolyte dataset, comprising six LiTFSI/G_3 molar fractions, as reported by Wang *et al.* [30]. The analysis was performed using the PYNEP code [31]. The two principal components are visualized with a color bar, where higher values indicate greater projection density. Black dots denote 154 sparsely selected structures, ensuring configurational diversity and data efficiency.

The numbers of input layer descriptors and hidden layer neurons are denoted as N_{des} and N_{neu} , respectively.

The descriptor vector \mathbf{q}^i in NEP typically comprises radial (2-body) and angular (many-body) components, conceptually similar to Behler-Parrinello symmetry functions [39] and the optimized smooth overlap of atomic positions (SOAP) [40, 41]. The 2-body terms q_n^i are expressed as a sum of radial basis functions $g_n(r_{ij})$:

$$q_n^i = \sum_{j \neq i} g_n(r_{ij}), \quad 0 \leq n \leq n_{\text{max}}^{\text{R}}. \quad (2)$$

Here, r_{ij} is the distance between atoms i and j , and each $g_n(r_{ij})$ is expanded as a linear combination of Chebyshev polynomials.

The angular descriptor components capture 3-body and 4-body correlations using spherical harmonics. The 3-body terms q_{nl}^i ($0 \leq n \leq n_{\text{max}}^{\text{A}}$, $1 \leq l \leq l_{\text{max}}$) are defined as:

$$q_{nl}^i = \frac{2l+1}{4\pi} \sum_{j \neq i} \sum_{k \neq i} g_n(r_{ij}) g_n(r_{ik}) P_l(\cos \theta_{ijk}), \quad (3)$$

where θ_{ijk} denotes the angle between atomic pairs ij and ik , and P_l represents the Legendre polynomial. In

NEP implementations, the radial functions used in 3-body components may have a distinct cutoff radius r_c^A from that in 2-body components r_c^R .

C. Trained NEP model

TABLE I. Hyperparameters used for training the NEP model on LiTFSI/G₃.

Parameter	Value	Parameter	Value
r_c^R	6 Å	r_c^A	6 Å
n_{\max}^R	10	n_{\max}^A	10
N_{bas}^R	8	N_{bas}^A	8
l_{\max}^{3b}	4	l_{\max}^{4b}	2
N_{neu}	30	N_{gen}	1.3×10^6
λ_e	1.0	ZBL	2.5 Å
λ_f	1.0	λ_v	0.1
N_{bat}	490	N_{pop}	50

The trainable parameters are optimized using SNES [38] to minimize a loss function comprising a weighted sum of the root-mean-square errors (RMSEs) of energy, force, and virial stress over N_{gen} generations with a population size of N_{pop} . The radial (r_c^R) and angular (r_c^A) cutoffs influence the accuracy of the NEP model. After careful testing, we selected $r_c^R = r_c^A = 6$ Å as the optimal choice. To capture many-body interactions in the LiTFSI/G₃ system, we incorporated a single 4-body descriptor with $l_{\max}^{4b} = 2$. Additionally, the universal pair potential by Ziegler, Biersack, and Littmark (ZBL) [42] was applied with a cutoff of 2.5 Å to enhance short-range repulsion, improving the robustness of the trained model. We employed the NEP4 version [21] to train our model using a full-batch approach. All hyperparameters used in training are listed in Table I.

Figure 3 presents the parity plots for physical quantities, including energy, force, and virial stress, as predicted by the trained NEP model against DFT references. The results indicate that our NEP model for LiTFSI/G₃ achieves near-quantum mechanical accuracy in both the training set (light green dots) and the test set, which consists of 60 CMD configurations (orange dots) and 66 PIMD configurations (blue dots). Specifically, the reported RMSEs for the training set are 0.5 meV/atom for energy (Fig. 3(a)), 86.9 meV/Å for force (Fig. 3(b)), and 11.2 meV/atom for virial stress (Fig. 3(c)).

While the CMD test set exhibits accuracy comparable to the training set (and even surpasses it in force prediction, with an RMSE of 64 meV/Å compared to 86.9 meV/Å for the training set), the PIMD test set shows relatively lower accuracy, with a larger energy RMSE of 1.9 meV/atom and a higher force RMSE of 110.6 meV/Å. The higher RMSE values in the PIMD test set may be attributed to the broader configurational diversity in PIMD simulations, which exhibit a wider energy and force distribution in Fig. 3(a-b) compared to

the CMD test set.

D. Computational details

In the LiTFSI/G₃ electrolyte system, the solute concentration of LiTFSI plays a crucial role in the diffusion behavior of Li⁺. To investigate this effect, we systematically studied electrolyte systems across a broad range of solute molar ratios, including LiTFSI/G₃ = 0 (pure G₃), 0.0625, 0.20, 0.36, 0.58, 0.82, and 1. Each system consists of approximately 500 atoms. A structural snapshot of the solute-to-solvent molar ratio LiTFSI/G₃ = 1 is shown in Fig. 1. All molecular dynamics (MD) simulations in this study were performed using $3 \times 3 \times 3$ supercells, with atom counts ranging from 12,000 to 15,000. Detailed structural information for LiTFSI/G₃ supercells at different molar ratios is provided in Table II.

TABLE II. Structural details of electrolyte supercells with different LiTFSI/G₃ molar ratios at 300 K, including system size (nm), number of atoms (N_{atoms}), number of solute LiTFSI molecules (N_{LiTFSI}), number of solvent G₃ molecules (N_{G_3}), Li⁺ concentration ($c(\text{Li}^+)$ in mol L⁻¹), and mass densities (kg L⁻¹) from this work and available experimental data [43].

LiTFSI/G ₃	Size	N_{atoms}	N_{G_3}	N_{LiTFSI}	$c(\text{Li}^+)$	ρ_{MD}	ρ_{Exp}
0	52.89	14,580	486	0	0	0.999	0.986
0.0625	51.75	13,392	432	27	0.319	1.044	–
0.20	52.20	13,446	405	81	0.849	1.137	–
0.36	52.80	13,500	378	135	1.279	1.222	–
0.58	52.61	12,744	324	189	1.682	1.328	–
0.82	53.28	12,798	297	243	1.982	1.400	–
1.00	53.63	12,420	270	270	2.149	1.414	1.420

Using classical molecular dynamics (CMD) and path-integral molecular dynamics (PIMD), we systematically calculated various electrolyte properties at different concentrations and temperatures, including density, coordination environment, viscosity, and self-diffusion coefficients. For density calculations, electrolyte structures were equilibrated for 2 ns in the NPT ensemble using a stochastic cell rescaling thermostat [44], with density values averaged over the final 1 ns of the trajectory. PIMD simulations included 1 ns of equilibration followed by 0.5 ns of statistical averaging. Pair correlation functions (PCFs) were computed from the equilibrated trajectories.

Viscosity was determined by averaging over 30 independent simulations, each consisting of 2 ns of NPT equilibration followed by 1 ns of NVE simulation with a correlation time of 200 ps. Self-diffusion coefficients were averaged over three independent runs, each comprising 2 ns of NPT equilibration and 2 ns of NVT simulation using a Nosé-Hoover chain thermostat, with a correlation time of 20 ps. For PIMD simulations, after 0.5 ns of NPT equilibration, an additional 0.5 ns was used for property calculations. The computation of the velocity autocorre-

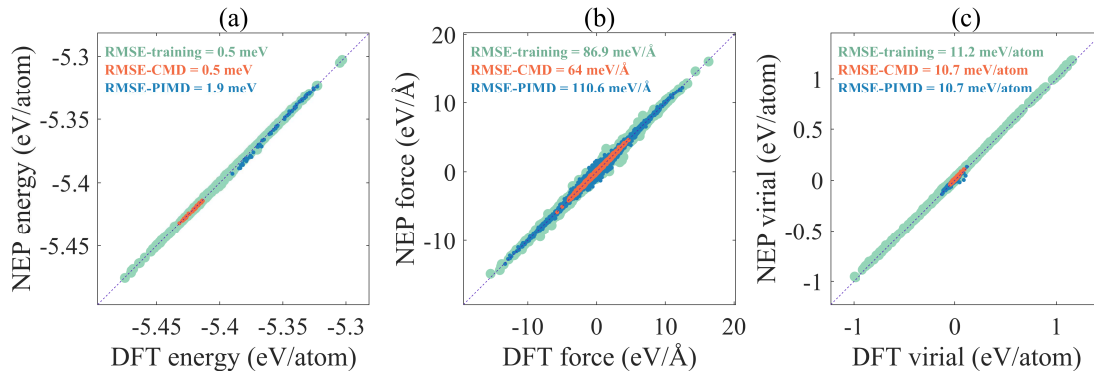


FIG. 3. Parities of (a) energies, (b) forces, and (c) virials predicted by NEP as against DFT reference values. The training set (490 configurations) is shown in light green, while the test sets include 60 CMD configurations (orange) and 66 PIMD configurations (blue). The RMSE values for each dataset are provided in the corresponding panels.

lation function (VAC) in PIMD followed the same procedure as in CMD.

All calculations based on the NEP model were performed using the GPUMD package [45], while DP model simulations were conducted in LAMMPS [46]. The time step was set to 1 fs for CMD and 0.5 fs for PIMD. All MD simulations incorporated D3 dispersion corrections.

III. RESULTS AND DISCUSSION

A. Electrolyte structure

LiTFSI serves as the electrolyte salt, and G_3 as the solvent, both of which possess symmetrical chain-like structures. In the LiTFSI molecular chain, the terminal CF_3 groups are symmetrically positioned and covalently bonded to sulfur atoms (depicted as larger orange atoms in Fig. 1(c)). Each sulfur atom is further doubly bonded to two oxygen atoms (shown as red spheres), which are located on either side of the molecular backbone. The two symmetric CF_3SO_2 groups are collectively bonded to a central nitrogen atom. In pure LiTFSI molecules, Li atoms preferentially reside near the central nitrogen atom, coordinating with the surrounding oxygen atoms.

The G_3 molecule adopts a long chain-like structure composed of carbon, oxygen, and hydrogen atoms, as illustrated in Fig. 1(a). The molecular chain is terminated by a methoxy (CH_3O-) group at one end and a methyl (CH_3-) group at the other, while the backbone consists of three repeating CH_2CH_2O- units.

As shown in Fig. 1(b), Li^+ ions (marked in green) coordinate with four oxygen atoms and are surrounded by G_3 molecules. Notably, these oxygen atoms originate from both individual G_3 molecules and the surrounding G_3 electrolyte. Specifically, Li^+ can coordinate with oxygen atoms from multiple G_3 molecules and may also interact with oxygen atoms in TFSI $^-$ anions, as depicted in Fig. 1(d-e). This multi-coordination behavior gives rise

to a more complex local chemical environment for Li^+ , significantly influencing its solvation structure and dynamic diffusion behavior.

B. Density

Both our tests and the study by Wang et al. [30] have emphasized the critical role of vdW interactions in the strongly polarized LiTFSI/ G_3 system, where long-range dispersion forces are essential for accurately predicting structural properties such as density. Under CMD calculations with D3 corrections, Fig. 4(a) presents the density as a function of the mole fraction of LiTFSI/ G_3 at room temperature. Since the electrolyte LiTFSI is denser than the solvent G_3 , an increase in LiTFSI/ G_3 concentration intuitively leads to higher density. Additionally, due to positive thermal expansion, higher temperatures result in lower-density structures.

Due to quantum effects in the electrolyte, PIMD simulations were performed. PIMD employs a quantum mechanical formulation in which quantum particles are represented as "strings" or "paths" composed of classical particles. By leveraging the path integral approach, PIMD effectively captures quantum behavior, providing a more accurate representation of quantum effects [48–50]. This method is particularly effective in capturing quantum fluctuations, making it a valuable tool for studying quantum systems. However, compared to CMD, PIMD entails significantly higher computational costs due to the additional degrees of freedom introduced by path integration. To balance computational accuracy and efficiency, we employ 32 "strings" to represent each particle in this study.

Figure 4(b) presents the density-concentration relationship for LiTFSI/ G_3 solutions at room temperature, as calculated using CMD and PIMD. For comparison, data from DP-driven CMD simulations [30] and experimental measurements [43, 47] are also included. The

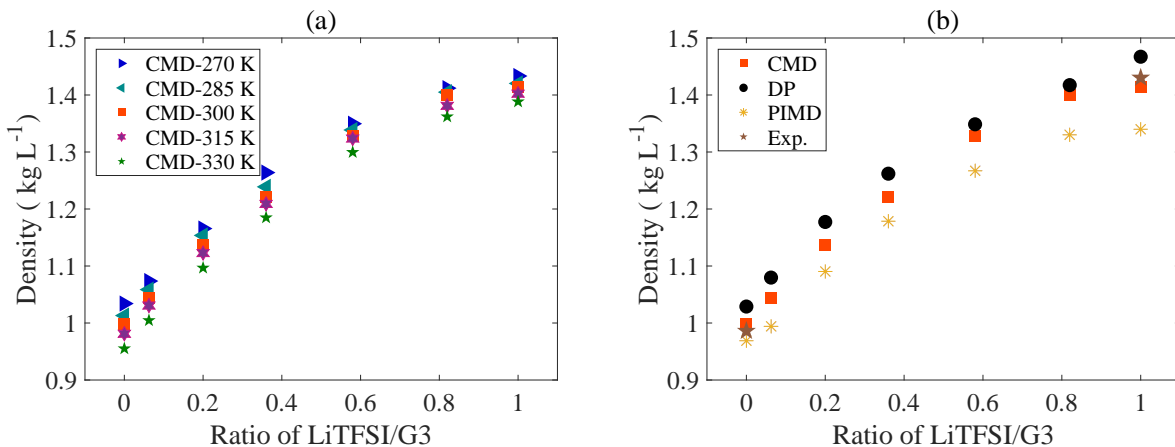


FIG. 4. Density as a function of LiTFSI/G₃ molar fraction (0–1): (a) CMD predictions over a temperature range of 270–330 K, and (b) comparison of NEP-driven PIMD, NEP-driven CMD, and DP-driven CMD [30] calculations with experimental measurements [43, 47] at 300 K.

results show that our NEP-driven CMD calculations are in good agreement with DP simulations and exhibit even better consistency with experimental data at LiTFSI/G₃ ratios of 0 and 1. Furthermore, due to quantum fluctuations, PIMD predicts lower densities compared to CMD while still maintaining good agreement with experimental results.

C. Pair correlation function

Since the motion of Li⁺ is influenced by nearby oxygen atoms in the LiTFSI/G₃ electrolyte, we analyzed the pair correlation function (PCF) for Li–O pairs at different Li⁺/G₃ ratios, as shown in Fig. 5. Regardless of Li⁺ concentration, a sharp peak at $r_1 \approx 2.2$ Å indicates a strong Li–O interaction. The oxygen atoms originate from both the solute LiTFSI and the solvent G₃. Li⁺ interacts not only with oxygen atoms bonded to sulfur in solute LiTFSI but also with those from the ether and glycol groups of solvent G₃.

Additionally, a weak PCF peak appears at $r_2 \approx 4.5$ Å, with its intensity increasing significantly as the Li⁺/G₃ ratio rises. This observation is in good agreement with CMD simulation results reported by Wang et al. [30]. The peak corresponds to the second coordination shell of Li⁺ and primarily originates from oxygen atoms in solute LiTFSI molecules. In LiTFSI, each sulfur atom forms bonds with two oxygen atoms, resulting in an O–S–O triplet. Li⁺ ions coordinate asymmetrically, favoring one side of the LiTFSI molecular chain. This leads to a configuration where Li⁺ binds to proximal oxygen atoms in the triplets at $r_1 \approx 2.2$ Å and coordinates with distal oxygen atoms at $r_2 \approx 4.5$ Å. These two peaks suggest local chemical ordering in the first and second Li–O coordination shells. This structural feature significantly influences the dynamic diffusion behavior of Li⁺ [51]. Furthermore, the alignment of PCF distributions between

CMD and PIMD (Fig. 5) indicates that quantum effects have a negligible impact on Li–O coordination.

D. Viscosity

Viscosity plays a crucial role in the diffusion behavior of Li⁺ in the LiTFSI/G₃ electrolyte. Therefore, we investigate the viscosity of electrolytes with LiTFSI/G₃ mole ratios ranging from 0 to 1. Viscosity can be essentially categorized into shear viscosity and longitudinal viscosity. Shear viscosity characterizes the resistance encountered by fluid layers during relative motion, while longitudinal viscosity quantifies the internal frictional resistance of the fluid during compression or expansion.

The viscosity was calculated using the stress autocorrelation function,

$$\eta_{\alpha\beta}(t) = \frac{1}{k_B T V} \int_0^t \langle S_{\alpha\beta}(0) S_{\alpha\beta}(t') \rangle dt', \quad (4)$$

where $S_{\alpha\beta}$ represents the stress tensor components ($\alpha, \beta = x, y, z$), t is the correlation time, $\langle \cdot \rangle$ denotes the ensemble average, k_B is the Boltzmann constant, T is the temperature, and V is the system volume.

The longitudinal viscosity is computed as the average of three independent diagonal components:

$$\eta_L = \frac{\eta_{xx} + \eta_{yy} + \eta_{zz}}{3}. \quad (5)$$

Similarly, the shear viscosity is obtained by averaging the corresponding off-diagonal components:

$$\eta_S = \frac{\eta_{xy} + \eta_{yz} + \eta_{zx}}{3}. \quad (6)$$

Finally, the bulk viscosity is expressed as a function of the longitudinal and shear viscosities:

$$\eta_B = \eta_L - \frac{4}{3}\eta_S. \quad (7)$$

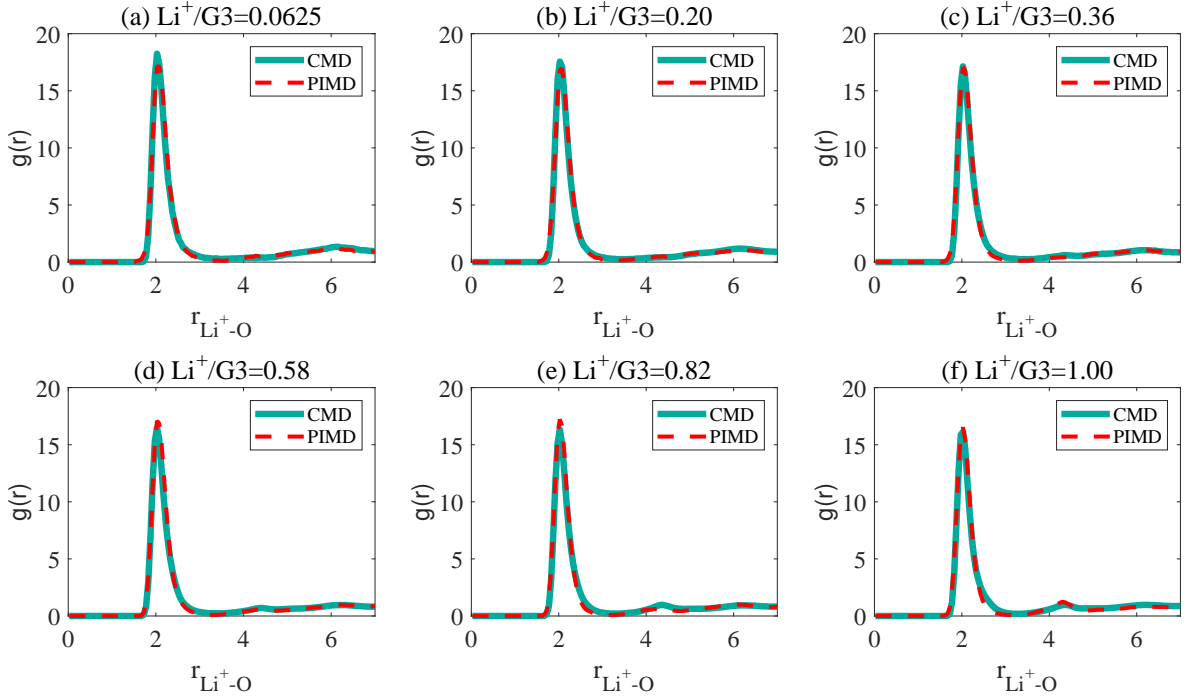


FIG. 5. Pair correlation function $g(r)$ for Li–O interactions in LiTFSI/G₃ at 300 K, shown as a function of Li–O distance for different Li⁺/G₃ molar fractions: (a) 0.0625, (b) 0.2, (c) 0.36, (d) 0.58, (e) 0.82, and (f) 1. CMD and PIMD results are presented for comparison.

Figure 6 illustrates the time-correlated η_L and η_S curves for the electrolyte with LiTFSI/G₃ = 1, where 30 independent runs were performed to obtain statistical averages. The converged η_L and η_S values at different LiTFSI/G₃ ratios, along with the derived bulk viscosity η_B , are shown in Fig. 7. A positive correlation is observed between viscosity and Li⁺ concentration [52], indicating that Li⁺ enhances shear, longitudinal, and bulk viscosities. This effect is primarily attributed to the role of Li⁺ in the electrolyte, where solute and solvent oxygen atoms in the vicinity of Li⁺ interact strongly with it. Such interactions between the solute LiTFSI and solvent G₃ hinder the dynamic flow of the fluid.

E. Self diffusion for lithium ions

In this section, we employ two distinct approaches to compute the self-diffusion coefficient (D). The first method derives D from the time-dependent mean squared displacement (MSD) in the limit of large correlation time:

$$\begin{aligned} D_{\text{MSD}}(t) &= \frac{1}{6} \lim_{t \rightarrow \infty} \frac{d}{dt} \text{MSD}(t) \\ &= \frac{1}{6} \lim_{t \rightarrow \infty} \frac{d}{dt} \langle [\mathbf{r}(t) - \mathbf{r}(0)]^2 \rangle, \end{aligned} \quad (8)$$

where $\mathbf{r}(t)$ denotes the position of Li⁺ at time t .

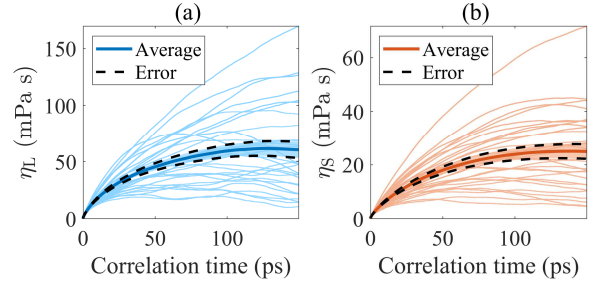


FIG. 6. CMD-derived (a) longitudinal and (b) shear viscosities versus correlation time for the LiTFSI/G₃ electrolyte at LiTFSI/G₃ = 1. Statistical averages were obtained from 30 independent runs, with standard errors shown in each panel.

An alternative approach estimates D using the velocity autocorrelation function (VAC):

$$D_{\text{VAC}}(t) = \frac{1}{3} \int_0^t \langle \mathbf{v}(0) \cdot \mathbf{v}(t') \rangle dt', \quad (9)$$

where \mathbf{v} represents the velocity of Li⁺, and $\langle \cdot \rangle$ denotes the ensemble average.

Figure 8 presents the self-diffusion behavior of Li⁺ in the electrolyte. We first computed the mean squared displacement (MSD) as a function of correlation time for LiTFSI/G₃ = 0.0625, as shown in Fig. 8(a). Our NEP

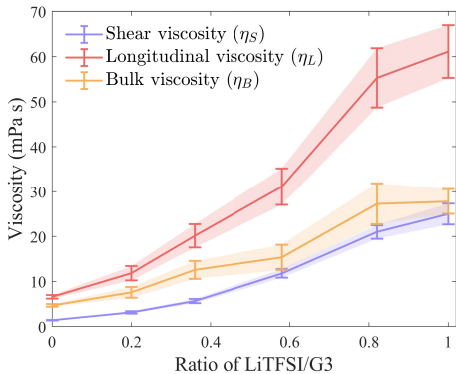


FIG. 7. Converged viscosity as a function of LiTFSI/G₃ concentration at 300 K. Statistical averages were obtained from 30 independent runs, with standard errors shown in each panel.

model predicts a higher MSD trend compared to the DP model in CMD simulations. This difference is attributed to the mass density of the electrolyte, as the DP model overestimates the density (see Fig. 4(b)), resulting in a denser LiTFSI/G₃ system where the diffusion of Li⁺ is hindered.

The derivatives of $\text{MSD}(t)$, corresponding to the self-diffusion coefficient D_{MSD} , are plotted in Fig. 8(b) alongside the D_{VAC} values obtained from the velocity autocorrelation function in Eq. 9. Due to the steeper slope in Fig. 8(a), the MSD-derived D_{MSD} from our NEP model is higher than that predicted by the DP model. Moreover, the near-perfect alignment between the $D_{\text{MSD}}(t)$ and $D_{\text{VAC}}(t)$ curves confirms the equivalence of the two methods for computing self-diffusion in CMD simulations. Furthermore, the consistency between CMD and PIMD calculations in Fig. 8(b) indicates that quantum effects have a negligible impact on the self-diffusion behavior of Li⁺ in electrolytes with low Li⁺ concentrations.

By extracting the converged values of $D(t)$ at long correlation times, we further investigate the effects of temperature and Li⁺ concentration on the self-diffusion coefficient of Li⁺ in the LiTFSI/G₃ electrolyte. As shown in Fig. 8(c), Li⁺ exhibits a linear inverse correlation between D and temperature, following a $D \propto T^{-1}$ dependence for LiTFSI/G₃ = 1. As expected, higher temperatures facilitate diffusion, resulting in larger D values. The NEP-predicted $D \propto T^{-1}$ trend in the LiTFSI/G₃ system is in good agreement with DP-calculated results, previous MD simulations of LiTFSI/G₄ electrolytes [54], and experimental measurements of a 1 M LiTf/G₃ system [26].

In addition, Li⁺ exhibits a similar dependence on LiTFSI concentration at 300 K. As shown in Fig. 8(d), increasing the LiTFSI ratio suppresses diffusion. Combined with the viscosity analysis in Sec. III D, this trend suggests that a higher LiTFSI mole fraction strengthens the interactions between Li⁺ and neighboring oxygen atoms

in both solute LiTFSI and solvent G₃ (see Fig. 5), thereby hindering Li⁺ diffusion. Furthermore, self-diffusion exhibits visible quantum effects at higher Li⁺ concentrations, despite the negligible difference observed at lower concentrations. Moreover, the DP model consistently underestimates self-diffusion coefficients with respect to both temperature and Li⁺ concentration due to its overestimation of density.

IV. CONCLUSIONS

In this study, we developed a high-accuracy neuroevolution potential (NEP) for the LiTFSI/G₃ (LiTFSI-G₃) electrolyte and applied it to large-scale molecular dynamics simulations. By employing an active learning strategy, we constructed a dataset encompassing diverse electrolyte configurations, enabling the NEP model to achieve near-DFT accuracy while maintaining computational efficiency. The model was validated against benchmark DFT calculations, demonstrating excellent predictive performance for energies, forces, and virial stresses.

Using this NEP model, we systematically investigated the structural and transport properties of the electrolyte, including density, ion coordination, viscosity, and Li⁺ self-diffusion. The computed densities closely matched experimental measurements, with PIMD simulations further confirming the minor role of quantum effects in this system. Pair correlation function analysis revealed that Li⁺ coordination involves both solvent G₃ and solute LiTFSI, influencing its dynamic behavior. Viscosity calculations indicated that increasing LiTFSI concentration strengthens ion-ion interactions, leading to higher viscosity and reduced Li⁺ mobility. Self-diffusion coefficients exhibited a clear dependence on both temperature and concentration, aligning well with experimental trends. These findings establish NEP as a robust and efficient framework for accurately modeling electrolyte behavior and gaining deeper insights into ion transport mechanisms.

Data availability: Complete input and output files for the NEP training and testing are freely available at a Zenodo repository [55].

ACKNOWLEDGMENTS

Y.S. appreciates the support received from the Fundamental Research Funds for the Central Universities (FRF-TP-22-106A1). C.C. and P.Q. acknowledge the support from the National Key Research and Development Program of China (2021YFB3802104). We acknowledge the computational resources provided by High Performance Computing Platform of Beijing Advanced Innovation Center for Materials Genome Engineering.

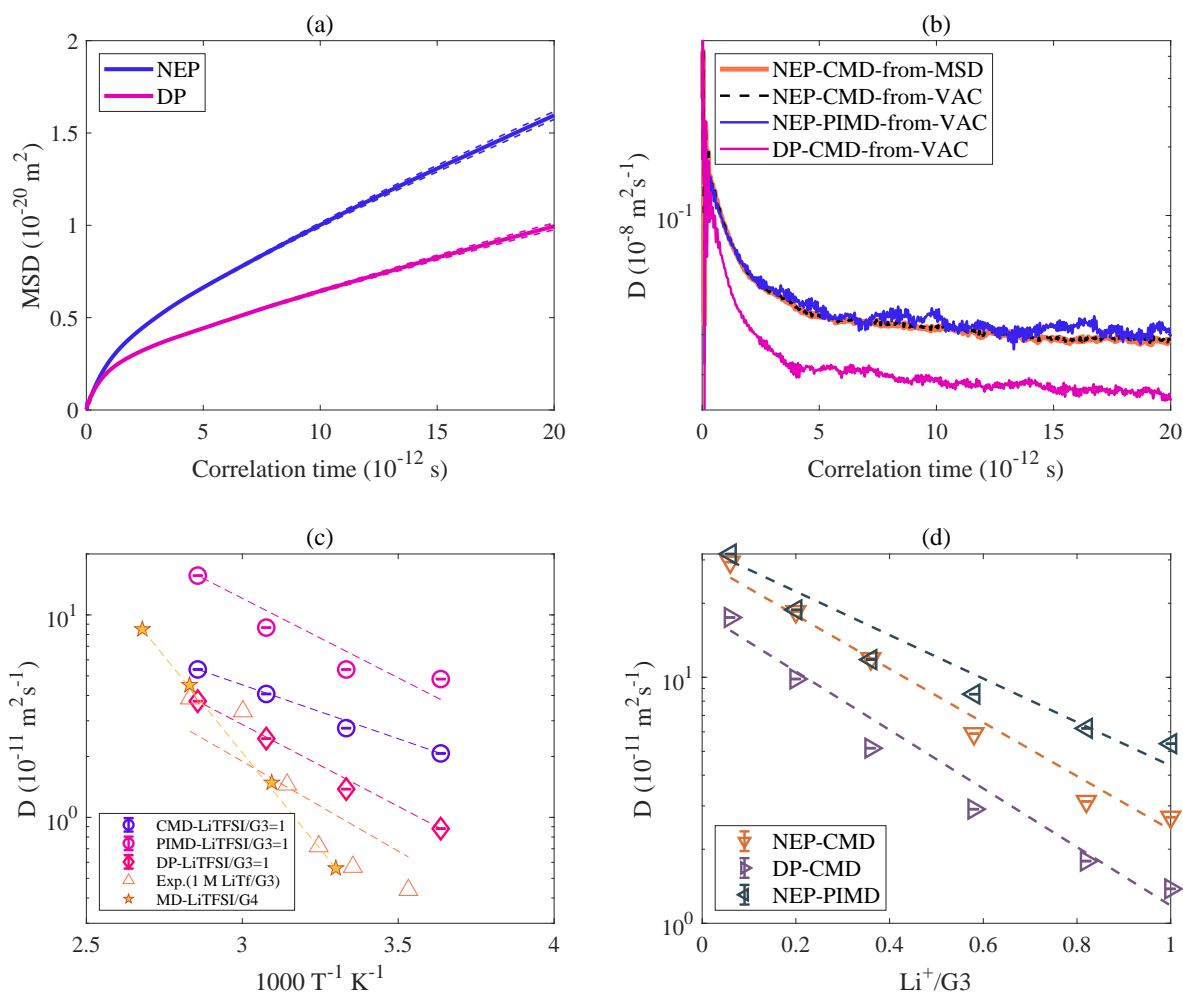


FIG. 8. Self-diffusion of Li⁺ in LiTFSI/G₃. (a) CMD-calculated mean squared displacement versus correlation time for LiTFSI/G₃ = 0.0625 at 300 K. (b) Self-diffusion coefficients for LiTFSI/G₃ = 0.0625 at 300 K, derived from mean squared displacement and velocity autocorrelation methods. CMD-NEP, PIMD-NEP, and CMD-DP results are compared. (c) Self-diffusion coefficient as a function of inverse temperature for LiTFSI/G₃ = 1. (d) Self-diffusion coefficient as a function of Li⁺ concentration at 300 K. Experimental data for 1 M LiTf/G₃ [26] and CMD simulations for LiTFSI/G₄ = 1 [53] are provided for reference.

-
- [1] P.-Y. Yang and C.-W. Pao, Molecular simulations of the microstructure evolution of solid electrolyte interphase during cyclic charging/discharging, *ACS Applied Materials & Interfaces* **13**, 5017 (2021), PMID: 33467849, <https://doi.org/10.1021/acsami.0c18783>.
- [2] T. Wulandari, D. Fawcett, S. B. Majumder, and G. E. Poinern, Lithium-based batteries, history, current status, challenges, and future perspectives, *Battery Energy* **2**, 20230030 (2023).
- [3] C. Wang, Y. Yang, X. Liu, H. Zhong, H. Xu, Z. Xu, H. Shao, and F. Ding, Suppression of lithium dendrite formation by using lagp-peo (litfsi) composite solid electrolyte and lithium metal anode modified by peo (litfsi) in all-solid-state lithium batteries, *ACS Applied Materials & Interfaces* **9**, 13694 (2017), PMID: 28334524, <https://doi.org/10.1021/acsami.7b00336>.
- [4] H.-M. Kwon, M. L. Thomas, R. Tatara, Y. Oda, Y. Kobayashi, A. Nakanishi, K. Ueno, K. Dokko, and M. Watanabe, Stability of glyme solvate ionic liquid as an electrolyte for rechargeable li-o₂ batteries, *ACS Applied Materials & Interfaces* **9**, 6014 (2017), PMID: 28121136, <https://doi.org/10.1021/acsami.6b14449>.
- [5] Y. Lu, S. Yan, Y. He, Z. Liu, X. Ma, Y. Ou, W. Zhang, and K. Liu, Understanding and tuning intermolecular interactions of the electrolyte solvation structure for low-temperature lithium-based batteries, *Energy Storage Materials* **72**, 103741 (2024).
- [6] M. Gauthier, T. J. Carney, A. Grimaud, L. Giordano, N. Pour, H.-H. Chang, D. P. Fenning, S. F. Lux, O. Paschos, C. Bauer, *et al.*, Electrode-electrolyte interface in li-ion batteries: current understanding and new insights, *The journal of physical chemistry letters* **6**, 4653 (2015).
- [7] L. Bai, S. Ghiassinejad, J. Brassinne, Y. Fu,

- J. Wang, H. Yang, A. Vlad, A. Minoia, R. Lazaroni, and J.-F. Gohy, High salt-content plasticized flame-retardant polymer electrolytes, *ACS Applied Materials & Interfaces* **13**, 44844 (2021), PMID: 34505760, <https://doi.org/10.1021/acsami.1c11058>.
- [8] M. Ilikso, A. Khetan, S. Yang, U. Simon, H. Pitsch, and D. U. Sauer, Elucidation and comparison of the effect of litfsi and lino3 salts on discharge chemistry in nonaqueous li-o2 batteries, *ACS Applied Materials & Interfaces* **9**, 19319 (2017), PMID: 28485949, <https://doi.org/10.1021/acsami.7b03592>.
- [9] D. Dong, F. Sälzer, B. Roling, and D. Bedrov, How efficient is Li+ ion transport in solvate ionic liquids under anion-blocking conditions in a battery?, *Phys. Chem. Chem. Phys.* **20**, 29174 (2018).
- [10] M. Rezaei, S. Sakong, and A. Groß, Sodium triflate water-in-salt electrolytes in advanced battery applications: A first-principles-based molecular dynamics study, *ACS Applied Materials & Interfaces* **16**, 32169 (2024), PMID: 38862108, <https://doi.org/10.1021/acsami.4c01449>.
- [11] P. Johansson, Electronic structure calculations on lithium battery electrolyte salts, *Phys. Chem. Chem. Phys.* **9**, 1493 (2007).
- [12] G. Agarwal, J. D. Howard, V. Prabhakaran, G. E. Johnson, V. Murugesan, K. T. Mueller, L. A. Curtiss, and R. S. Assary, Insights into spontaneous solid electrolyte interphase formation at magnesium metal anode surface from ab initio molecular dynamics simulations, *ACS Applied Materials & Interfaces* **13**, 38816 (2021), PMID: 34362250, <https://doi.org/10.1021/acsami.1c07864>.
- [13] M. Yang, U. Raucci, and M. Parrinello, Reactant-induced dynamics of lithium imide surfaces during the ammonia decomposition process, *Nat. Catal* **6**, 829–836 (2023).
- [14] W. Wang, T. Yang, W. H. Harris, and R. Gómez-Bombarelli, Active learning and neural network potentials accelerate molecular screening of ether-based solvate ionic liquids, *Chem. Commun.* **56**, 8920 (2020).
- [15] T. Binninger, D. Saraç, L. Marsh, T. Picard, M.-L. Doublet, and C. Raynaud, AMOEBA Polarizable Force Field for Molecular Dynamics Simulations of Glyme Solvents, *Journal of Chemical Theory and Computation* **19**, 1023 (2023).
- [16] F. Wang, Y.-H. Tang, Z.-B. Ma, Y.-C. Jin, and J. Cheng, Soaring chemical space of battery electrolytes using universal machine learning potential, *ChemRxiv* [10.26434/chemrxiv-2025-fnw1w](https://doi.org/10.26434/chemrxiv-2025-fnw1w) (2025).
- [17] J. Lee, S. Ju, S. Hwang, J. You, J. Jung, Y. Kang, and S. Han, Disorder-dependent li diffusion in li6ps5cl investigated by machine-learning potential, *ACS Applied Materials & Interfaces* **16**, 46442 (2024), PMID: 39185625, <https://doi.org/10.1021/acsami.4c08865>.
- [18] Z. Fan, Z. Zeng, C. Zhang, Y. Wang, K. Song, H. Dong, Y. Chen, and T. Ala-Nissila, Neuroevolution machine learning potentials: Combining high accuracy and low cost in atomistic simulations and application to heat transport, *Phys. Rev. B* **104**, 104309 (2021).
- [19] Z. Fan, Improving the accuracy of the neuroevolution machine learning potential for multi-component systems, *Journal of Physics: Condensed Matter* **34**, 125902 (2022).
- [20] Z. Fan, Y. Wang, P. Ying, K. Song, J. Wang, Y. Wang, Z. Zeng, K. Xu, E. Lindgren, J. M. Rahm, A. J. Gabourie, J. Liu, H. Dong, J. Wu, Y. Chen, Z. Zhong, J. Sun, P. Erhart, Y. Su, and T. Ala-Nissila, Gpumd: A package for constructing accurate machine-learned potentials and performing highly efficient atomistic simulations, *The Journal of Chemical Physics* **157**, 114801 (2022).
- [21] K. Song, R. Zhao, J. Liu, Y. Wang, E. Lindgren, Y. Wang, S. Chen, K. Xu, T. Liang, P. Ying, *et al.*, General-purpose machine-learned potential for 16 elemental metals and their alloys, *Nature Communications* **15**, 10208 (2024).
- [22] P. Ying, C. Qian, R. Zhao, Y. Wang, K. Xu, F. Ding, S. Chen, and Z. Fan, Advances in modeling complex materials: The rise of neuroevolution potentials, *Chemical Physics Reviews* **6**, 011310 (2025).
- [23] Z. Yan and Y. Zhu, Impact of lithium nonstoichiometry on ionic diffusion in tetragonal garnet-type li7la3zr2o12, *Chemistry of Materials* **36**, 11551 (2024).
- [24] S. S. Zhang, A review on electrolyte additives for lithium-ion batteries, *Journal of Power Sources* **162**, 1379 (2006).
- [25] K. Yoshida, M. Nakamura, Y. Kazue, N. Tachikawa, S. Tsuzuki, S. Seki, K. Dokko, and M. Watanabe, Oxidative-stability enhancement and charge transport mechanism in glyme–lithium salt equimolar complexes, *Journal of the American Chemical Society* **133**, 13121 (2011).
- [26] M. Nojabae, J. Popovic, and J. Maier, Glyme-based liquid–solid electrolytes for lithium metal batteries, *J. Mater. Chem. A* **7**, 13331 (2019).
- [27] O. Carrillo-Bohórquez, D. G. Kuroda, and R. Kumar, A transferable classical force field to describe glyme based lithium solvate ionic liquids, *The Journal of Chemical Physics* **161**, 054504 (2024).
- [28] A. Lewandowski and A. Świdarska Mocek, Ionic liquids as electrolytes for li-ion batteries—an overview of electrochemical studies, *Journal of Power Sources* **194**, 601 (2009).
- [29] P. Ying, W. Zhou, L. Svensson, E. Berger, E. Fransson, F. Eriksson, K. Xu, T. Liang, J. Xu, B. Song, S. Chen, P. Erhart, and Z. Fan, Highly efficient path-integral molecular dynamics simulations with gpumd using neuroevolution potentials: Case studies on thermal properties of materials, *The Journal of Chemical Physics* **162**, 064109 (2025).
- [30] F. Wang and J. Cheng, Understanding the solvation structures of glyme-based electrolytes by machine learning molecular dynamics, *Chinese Journal of Structural Chemistry* **42**, 100061 (2023).
- [31] *Pynepe: A python package for neuroevolution potential* (2024), github repository, accessed on March 14, 2025.
- [32] G. Kresse and J. Furthmüller, Efficient iterative schemes for ab initio total-energy calculations using a plane-wave basis set, *Phys. Rev. B* **54**, 11169 (1996).
- [33] P. E. Blöchl, Projector augmented-wave method, *Phys. Rev. B* **50**, 17953 (1994).
- [34] G. Kresse and D. Joubert, From ultrasoft pseudopotentials to the projector augmented-wave method, *Phys. Rev. B* **59**, 1758 (1999).
- [35] J. P. Perdew, K. Burke, and M. Ernzerhof, Generalized Gradient Approximation Made Simple, *Phys. Rev. Lett.* **77**, 3865 (1996).
- [36] P. Ying and Z. Fan, Combining the d3 dispersion correction with the neuroevolution machine-learned potential, *Journal of Physics: Condensed Matter* **36**, 125901 (2023).
- [37] S. Grimme, J. Antony, S. Ehrlich, and H. Krieg, A consistent and accurate ab initio parametrization of density functional disper-

- sion correction (dft-d) for the 94 elements h-pu, *The Journal of Chemical Physics* **132**, 154104 (2010).
- [38] T. Schaul, T. Glasmachers, and J. Schmidhuber, High Dimensions and Heavy Tails for Natural Evolution Strategies, in *Proceedings of the 13th Annual Conference on Genetic and Evolutionary Computation*, GECCO '11 (Association for Computing Machinery, New York, NY, USA, 2011) pp. 845–852.
- [39] J. Behler and M. Parrinello, Generalized Neural-Network Representation of High-Dimensional Potential-Energy Surfaces, *Phys. Rev. Lett.* **98**, 146401 (2007).
- [40] A. P. Bartók, R. Kondor, and G. Csányi, On representing chemical environments, *Phys. Rev. B* **87**, 184115 (2013).
- [41] M. A. Caro, Optimizing many-body atomic descriptors for enhanced computational performance of machine learning based interatomic potentials, *Phys. Rev. B* **100**, 024112 (2019).
- [42] J. F. Ziegler and J. P. Biersack, The stopping and range of ions in matter, in *Treatise on Heavy-Ion Science: Volume 6: Astrophysics, Chemistry, and Cosmic Rays*, edited by D. A. Bromley (Springer US, Boston, MA, 1985) pp. 93–129.
- [43] K. Ueno, K. Yoshida, M. Tsuchiya, N. Tachikawa, K. Dokko, and M. Watanabe, Glyme–lithium salt equimolar molten mixtures: Concentrated solutions or solvate ionic liquids?, *The Journal of Physical Chemistry B* **116**, 11323 (2012).
- [44] G. Bussi and M. Parrinello, Accurate sampling using langevin dynamics, *Phys. Rev. E* **75**, 056707 (2007).
- [45] Z. Fan, W. Chen, V. Vierimaa, and A. Harju, Efficient molecular dynamics simulations with many-body potentials on graphics processing units, *Computer Physics Communications* **218**, 10 (2017).
- [46] A. P. Thompson, H. M. Aktulga, R. Berger, D. S. Bolintineanu, W. M. Brown, P. S. Crozier, P. J. in 't Veld, A. Kohlmeyer, S. G. Moore, T. D. Nguyen, R. Shan, M. J. Stevens, J. Tranchida, C. Trott, and S. J. Plimpton, LAMMPS - a flexible simulation tool for particle-based materials modeling at the atomic, meso, and continuum scales, *Comp. Phys. Comm.* **271**, 108171 (2022).
- [47] A. Conesa, S. Shen, and A. Coronas, Liquid densities, kinematic viscosities, and heat capacities of some ethylene glycol dimethyl ethers at temperatures from 283.15 to 423.15 K, *International Journal of Thermophysics* **19**, 1343 – 1358 (1998), <https://doi.org/10.1006/ijtp.1998.078>.
- [48] M. Ceriotti, M. Parrinello, T. E. Markland, and D. E. Manolopoulos, Efficient stochastic thermostatting of path integral molecular dynamics, *The Journal of Chemical Physics* **133**, 124104 (2010).
- [49] T. Morresi, L. Paulatto, R. Vuilleumier, and M. Casula, Probing anharmonic phonons by quantum correlators: A path integral approach, *The Journal of Chemical Physics* **154**, 224108 (2021).
- [50] X. Liu and J. Liu, Path integral molecular dynamics for exact quantum statistics of multi-electronic-state systems, *The Journal of Chemical Physics* **148**, 102319 (2017).
- [51] M. Callsen, K. Sodeyama, Z. Futera, Y. Tateyama, and I. Hamada, The Solvation Structure of Lithium Ions in an Ether Based Electrolyte Solution from First-Principles Molecular Dynamics, *The Journal of Physical Chemistry B* **121**, 180 (2017).
- [52] S. Tobishima, H. Morimoto, M. Aoki, Y. Saito, T. Inose, T. Fukumoto, and T. Kuryu, Glyme-based nonaqueous electrolytes for rechargeable lithium cells, *Electrochimica Acta* **49**, 979 (2004).
- [53] D. Dong and D. Bedrov, Charge Transport in [Li(tetraglyme)][bis(trifluoromethane)sulfonimide] Solvate Ionic Liquids: Insight from Molecular Dynamics Simulations, *The Journal of Physical Chemistry B* **122**, 9994 (2018).
- [54] F. Yan, K. Mukherjee, M. Maroncelli, and H. J. Kim, Infrared Spectroscopy of Li+ Solvation in Diglyme: Ab Initio Molecular Dynamics and Experiment, *The Journal of Physical Chemistry B* **127**, 9191 (2023).
- [55] C. CAO, Structural and transport properties of litfsi/g3 electrolyte with machine-learned molecular dynamics, [10.5281/zenodo.15086398](https://doi.org/10.5281/zenodo.15086398) (2025).